Numerical modelling of a looped travelling wave thermoacoustic engine

Tze Yeung Cho[1*], Jingyuan Xu[2], Simone Hochgreb[1]
[1]Department of Engineering, University of Cambridge, Cambridge CB2 1PZ, England
[2]Institute of Microstructure Technology, Karlsruhe Institute of Technology, Karlsruhe 76344, Germany
[*]Corresponding author: zc282@cam.ac.uk

ABSTRACT

This article presents a two-dimensional axis-symmetric computational fluid dynamics (CFD) simulation of a three-stage travelling wave thermoacoustic engine using ANSYS FLUENT. The model incorporates porous media submodels to represent heat exchangers and regenerators, operating at a heating temperature of 600 K and an ambient temperature of 293 K, with helium as the working fluid stabilised around 3 MPa mean pressure. In comparison to traditional network models (NM), CFD yields accurate results in solving the flow field and captures higher-order details in the fluid domain.

Keywords: computational fluid dynamics (CFD), thermoacoustic, refrigeration, engine

1. INTRODUCTION

Thermoacoustics has been considered an alternative technology for sustainable energy generation and conversion using low temperature heat [1]. Such systems operate by converting thermal energy into acoustic work, without any moving parts. In thermoacoustic cooling systems, the acoustic work can be used to power an acoustic refrigeration system. A significant breakthrough in the efficiency of such systems was achieved by de Block et al. [2] by using the concept of travelling wave thermoacoustic systems, which demonstrate the potential for significantly improved efficiency.

Recent research on thermoacoustic devices has predominantly focused on achieving three key objectives: lowering the onset temperature, enhancing efficiency, and increasing the power-to-volume ratio. These factors are crucial for reducing overall costs and making the system commercially viable [3, 4]. Researchers have explored various configurations to attain these goals, such as utilising higher mean pressure and more compact core components [5, 6, 7, 8], incorporating liquid resonators to increase the momentum [9, 10], and introducing phase-changing materials to utilise their latent heat [11, 12]. Despite active research, the evolution of designs remains slow, and there is a large research gap to close before it is economically competitive with conventional cooling technology.

As the complexity of these systems grows, modelling them becomes increasingly challenging. While the one-dimensional network models (NM) using DELTAEC [13] have been employed for low-pressure conventional thermoacoustic systems, DELTAEC lacks the functionality needed for additional components. Researchers have explored various computational fluid dynamics (CFD) approaches to model thermoacoustic systems. This includes two-dimensional simulations of various travelling wave systems using commercial software [14, 15, 16], and one-dimensional simulations [17]. However, reliable validation of the thermoacoustic system design still has to be carried out using experiments, as one-dimensional systems lack the necessary detail to capture the fluid mechanical losses of variable device geometries. As computational resources become more efficient and affordable, further validation of one-dimensional models using CFD for designing novel thermoacoustic systems would, therefore, benefit the research efforts.

In this article, we present the configurations and initial findings of two-dimensional CFD calculations of a travelling wave thermoacoustic engine using the Reynolds-Averaged Navier-Stokes (RANS) method via ANSYS FLUENT [18], and compare it against an NM with the same heating and ambient gas-phase temperatures.

2. METHODOLOGY

2.1 System configuration

Fig. 1 illustrates a three-stage loop engine design used in the calculations. Each stage of the engine consists of a thermoacoustic core with a cone at each end and a reson-

This is a paper for 15th International Conference on Applied Energy (ICAE2023), Dec. 3-7, 2023, Doha, Qatar.

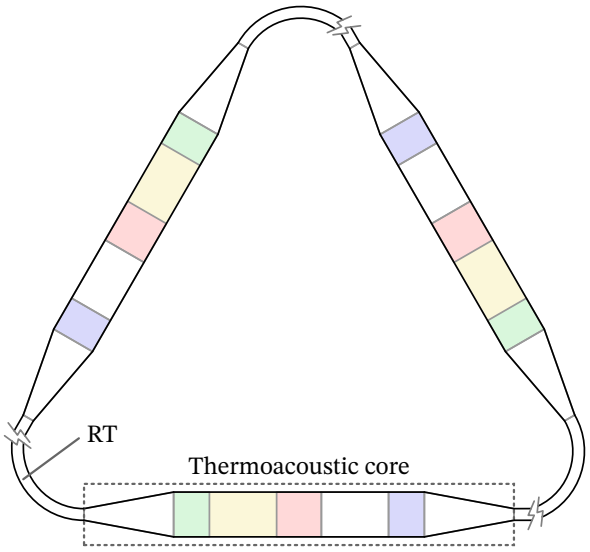

(a) Overall schematic of the thermoacoustic engine.

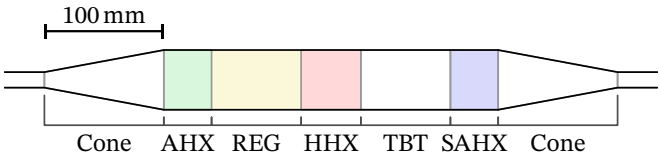

(b) Arrangements of the components in a thermoacoustic core.

Fig. 1. Schematics of the thermoacoustic engine system.

ance tube (RT). A thermoacoustic core is formed by connecting an ambient temperature heat exchanger (AHX), a regenerator (REG), a high-temperature heat exchanger (HHX), a thermal buffer tube (TBT), and a secondary AHX (SAHX) in series. Three identical stages are in turn connected to form a loop. This system is designed to operate around a heating temperature at 600 K, ambient temperature at 293 K, and mean operating pressure of helium working fluid at 3 MPa. The dimensions of the overall system and the corresponding heat exchanger parameters are listed in Tab. 1, where ϕ is porosity, r_h is hydraulic diameter, D_wir is wire diameter, and π_wal is wall thickness.

2.2 CFD model

We employ a finite volume commercial CFD solver, ANSYS FLUENT to conduct the simulation. The finite volume scheme solves for the balance of the set of conservation equations in each computational cell. In our simulation, the conservation of mass (1), momentum (2), and energy (3) [19] are employed as follows,

$$\frac{\partial}{\partial t}(\phi\rho) + \nabla\cdot(\phi\rho\boldsymbol{u}) = 0, \tag{1}$$

$$\frac{\partial}{\partial t}(\phi\rho\boldsymbol{u}) + \nabla\cdot(\phi\boldsymbol{u}\rho\boldsymbol{u}) = -\phi\nabla p + \nabla\cdot(\phi\boldsymbol{\sigma}) + \boldsymbol{S}_p, \tag{2}$$

$$\begin{aligned}\frac{\partial}{\partial t}(\phi\rho E_\mathrm{t}) + \nabla\cdot(\phi\boldsymbol{u}\rho E_\mathrm{t}) = \\ -\nabla\cdot(\phi p\boldsymbol{u}) + \nabla\cdot(\phi k\nabla T) + \nabla\cdot(\phi\boldsymbol{u}\cdot\boldsymbol{\sigma}) + S_q.\end{aligned} \tag{3}$$

In the conservation equations, velocity vector $\boldsymbol{u}$, density ρ, pressure p of the fluid, total energy E_t, temperature T, conductivity k, and viscous stress tensor $\boldsymbol{\sigma}$ are used. The correlation $\phi\boldsymbol{u}$ correlates the velocity to the volumetric flow rate per unit enclosure tube area (independent from porosity).

Porous media models are used to represent the heat exchangers and regenerators. A porous medium is mathematically constructed using a scalar porosity representing the fluid volume per unit volume of cell, and an associated velocity. The momentum source term $\boldsymbol{S}_p$ and energy source term S_q in the porous cells (both 0 in non-porous cells) are given as [18],

$$\boldsymbol{S}_p = -\left(\frac{\phi^2\mu}{\alpha}\boldsymbol{u} + \frac{\phi^3 C_2}{2}\rho|\boldsymbol{u}|\boldsymbol{u}\right), \tag{4}$$

$$S_h = h_\mathrm{fs}A_\mathrm{fs}(T_\mathrm{f} - T_\mathrm{s}), \tag{5}$$

where T_f, and T_s are the temperatures of fluid and solid zones. The inputs to the porous medium model are viscous resistance $1/\alpha$, inertial resistance C_2, heat transfer

Unit	Part	D [mm]	l [mm]	Other dimensions
Engine core	Cone	13 ↔ 50	100	Diameter changes linearly
	AHX	50	40	Plate-fin, $\phi = 20\%$, $r_\mathrm{h} = 0.5$ mm.
	REG		75	$\phi = 75\%$, $D_\mathrm{wir} = 52$ µm.
	HHX		50	Plate-fin, $\phi = 20\%$, $r_\mathrm{h} = 0.5$ mm.
	TBT		75	$\pi_\mathrm{wal} = 5$ mm.
	SAHX		40	Plated-fin, $\phi = 20\%$, $r_\mathrm{h} = 0.5$ mm.
Resonance tube	RT	13	3000	-

Tab. 1. Component dimensions and characteristics for simulation of the thermoacoustic engine.

Part	$\frac{1}{\alpha}$ [m^{-2}]	C_2 [m^{-1}]	A_{fs} [m^{-1}]	h_{fs} [W m^{-2} K^{-1}]
AHX	6×10^{7}	0	440	$\frac{\mathcal{N}u\,k}{4r_{\mathrm{h}}}$
REG	4.4×10^{9}	1.7×10^{4}	19 231	$\frac{\kappa_h Pr^{1/3} k}{4r_{\mathrm{h}}}\left(1+\mathcal{R}e^{\frac{4}{5}}\right)$
HHX	6×10^{7}	0	440	$\frac{\mathcal{N}u\,k}{4r_{\mathrm{h}}}$
SAHX	6×10^{7}	0	440	$\frac{\mathcal{N}u\,k}{4r_{\mathrm{h}}}$

Tab. 2. Values used for porous media configurations.

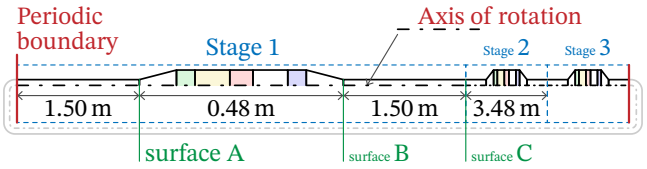

Fig. 2. Layout of the two-dimensional computational model (not drawn to scale, note that surface C is at the midpoint of an RT).

coefficient between fluid and solid h_{fs}, and interfacial area density (inverse length) between fluid and solid zones A_{fs}, which is defined by

$$A_{\mathrm{fs}} = \frac{\phi}{r_{\mathrm{h}}},$$

as a function of porosity ϕ and hydraulic diameter r_{h}. These values are listed in Tab. 2.

In Tab. 2, h_{fs} used the corrections between the non-dimensional Nusselt numbers $\mathcal{N}u$ and Reynolds numbers $\mathcal{R}e$. κ_h is a geometry correction function based on porosity [20]. In the REG tested [13],

$$\kappa_h = 3.81 - 11.29\phi + 9.47\phi^2,$$

$$r_{\mathrm{h,REG}} = D_{\mathrm{wir}}\frac{\phi}{4(1-\phi)},$$

and $\mathcal{N}u = 7.541$ in plate-fin heat exchangers [21].

To reduce computational costs, we simplify the three-dimensional loop of tube components to an axis-cylindrical CFD model. In this CFD model, the two-dimensional axis-cylindrical mesh consists of all three stages, and each end of this mesh is connected by a pair of periodic boundary conditions. The periodic boundary condition allows information to travel in the same manner as in a looped structure. The layout of a slice of the mesh is shown in Fig. 2. Other wall boundary conditions used in the CFD calculations are listed in Tab. 3.

The numerical scheme used for the CFD calculations is listed in Tab. 4. We apply pressure-implicit with splitting of

Zone	T_{w} [K]	q_{w} [W/m^2]	Wall material
AHX solid	298	-	Copper
AHX fluid	-	0	Copper
REG	-	0	Stainless steel
HHX solid	600	-	Copper
HHX fluid	-	0	Copper
TBT	-	0	Stainless steel
SAHX solid	298	-	Copper
SAHX fluid	-	0	Copper
Cone	298	-	Stainless steel
RT	298	-	Stainless steel

Tab. 3. Wall boundary conditions and configurations in the CFD model.

CFD software	FLUENT 2023 R1
Working fluid	Ideal helium, 3.0 MPa
Geometry space	Two-dimensional axis-symmetric
Transient formulation	Second-order implicit
p-v coupling	PISO, skewness correction = 0, neighbour correction = 1
Pressure differencing	PRESTO!
Spatial discretisation	Second-order upwind
Turbulence model	Realizable k–ϵ
Number of cells	18×10^{4}
Time-step size	5×10^{-4} s

Tab. 4. Numerical scheme used for the CFD calculations.

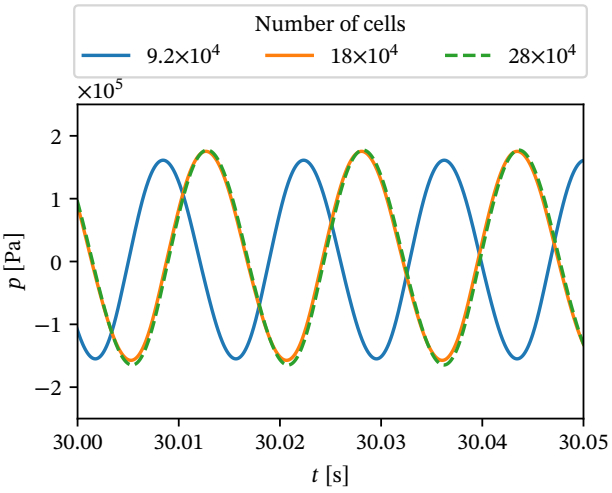

Fig. 3. Pressure oscillation at surface A with different numbers of cells.

operators (PISO) algorithm for pressure and velocity coupling, while disabling skewness correction due to its negative impact on transient results as a numerical source term. This combination ensures accuracy and efficiency in the computation. The realizable k–ϵ model calculates turbulence, providing a better solution in cases with large pressure gradients. Results from time and grid independence tests suggest that the tabulated cell size and time-step size yield the best results while utilising reasonable computational resources. The total number of cells is 18×10^4, with mean grid lengths of 1.0×10^{-3} m at core components and 1.5×10^{-3} m at RTs, while boundary cells are refined to around 1.5×10^{-4} m in length. Fig. 3 plots the pressure oscillation at surface A (location shown in Fig. 2) at different numbers of cells with finer and coarser mesh size settings. The change in pressure amplitude is minimal with further refinement beyond 18×10^4 cells.

2.3 NM configuration

The one-dimensional NM is constructed and solved with DELTAEC [13]. DELTAEC solves the linearised, periodic governing equations by assuming all oscillations are sinusoidal and at their primary resonance [22, 1]. It solves the one-dimensionalised perturbed equations in the frequency domain. It simplifies the model with radially-averaged properties [13, 22], the enthalpy of the fluid is unchanged in all components outside HXs, and no temperature gradient exists outside REG and TBT [23].

We use an equivalent NM model as a benchmark for comparison with CFD. In this equivalent model, the mean pressure is set to the CFD steady-state mean pressure, and the fluid temperature across each heat exchanger is assumed to be constant, matching the temporal and volumetric mean fluid temperature in the CFD of the respective heat exchanger.

3. RESULTS

Fig. 4 demonstrates the transient responses of the cross-sectional averaged values of pressure and volumetric flow rate during the establishing of steady-state acoustic oscillations between 0 s and 30 s, measured at surface A (location shown in Fig. 2). Contours of temperature T and axial velocity u_x during the onset process are illus-

$\overline{p}$ [Pa]	$\overline{T}_{\mathrm{AHX}}$ [K]	$\overline{T}_{\mathrm{HHX}}$ [K]	$\overline{T}_{\mathrm{SAHX}}$ [K]
3.11×10^6	324.1	532.7	355.9

Tab. 5. CFD steady-state averaged values in pressure and temperature.

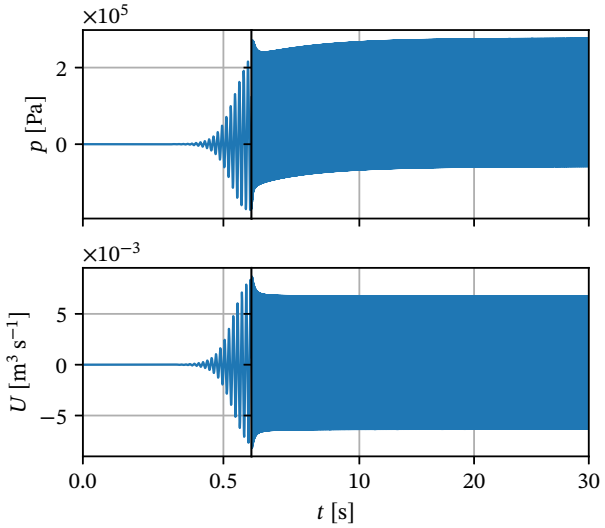

Fig. 4. Transient responses of pressure (offset from 3×10^6 Pa) and volumetric flow rate during the onset process measured at surface A.

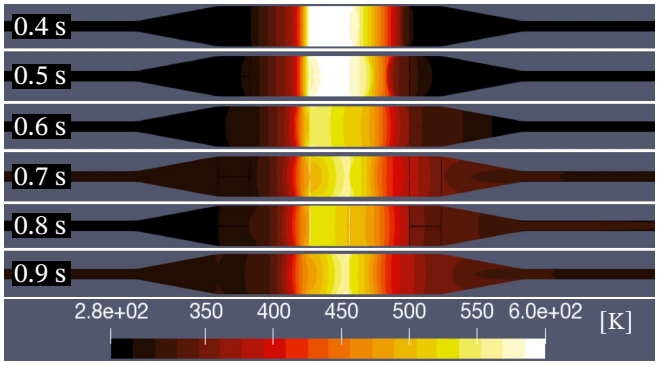

(a) Temperature at different times.

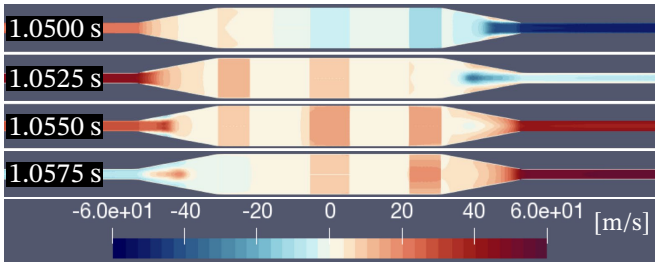

(b) Axial velocity at different times.

Fig. 5. Variables at different times during the onset process.

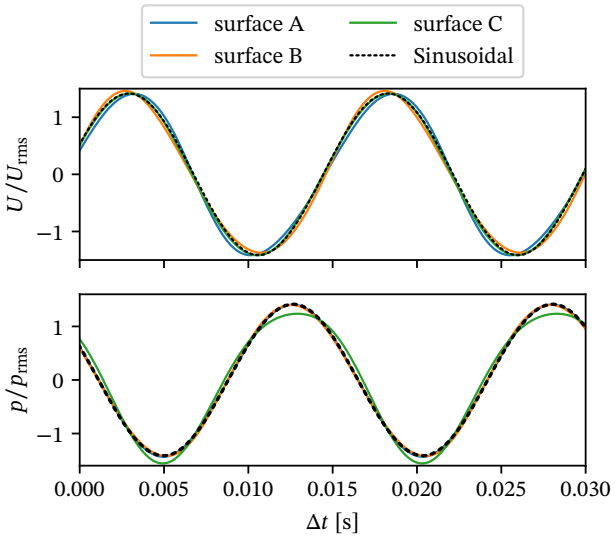

Fig. 6. Transient responses of volumetric flow rate and pressure oscillations at different locations compared to sinusoidal.

Method	f [Hz]	ΔE_{ac} [W]
CFD	65.00	101.90
NM	69.80	124.82

Method	Q_{AHX} [W]	Q_{HHX} [W]	Q_{SAHX} [W]
CFD	−636.33	2387.39	−1379.50
NM	−301.73	603.46	−301.73

Tab. 6. Steady-state averaged values in oscillation and thermal variables.

trated in Fig. 5. The amplitudes of perturbations amplify significantly between $t = 0.4\,\mathrm{s}$ and $t = 0.6\,\mathrm{s}$, indicating the triggering of acoustic oscillations. Subsequently, the amplitudes begin to reduce until around $t = 3\,\mathrm{s}$, due to the transient response of heat transfer to the establishing oscillating flow. The temperature in REG redistributes in response to the change in heat transfer and causes the mean pressure of oscillation to increase further until around $t = 20\,\mathrm{s}$. A steady-state oscillation is maintained after around $t = 20\,\mathrm{s}$.

Fig. 6 plots the normalised pressure and volumetric flow rate at steady-state, sampled at two oscillation periods, measured at surfaces A, B, and C (locations shown in Fig. 2), along with a fitted sinusoidal wave. The pressure oscillation near the core (surfaces A and B), and volumetric flow rate in RT (surface C) closely follow the sinusoidal wave, while the pressure in RT is non-sinusoidal. The volumetric flow rate at both cones is slanted due to the contraction and expansion flow area, and these effects can also be observed as the jets appear in Fig. 5.

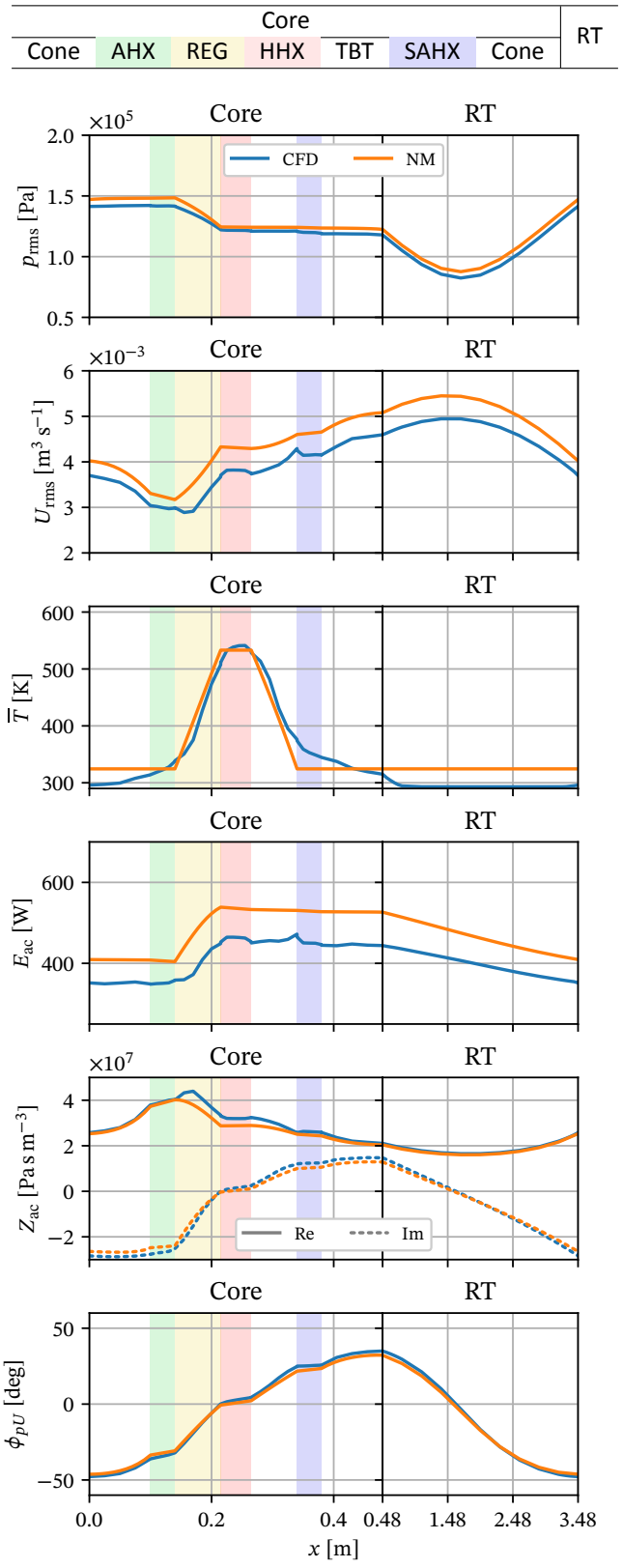

Fig. 7. Axial distribution of variables across one stage calculated by CFD and NM.

Tab. 5 lists the volumetric and temporal mean values of system pressure and heat exchanger component temperatures in working fluid when the system is under steady-state oscillation. These values are also used in the NM equivalent case for comparison.

The axial distributions of variables along a single stage, produced by both CFD calculations and NM, are plotted in Fig. 7. The axial distributions root mean square (rms) values of pressure p_{rms} and volumetric flow rate U_{rms}, closely match between CFD and equivalent NM. Volumetric flow rate U_{rms} experiences a small reduction near the boundary with AHX in REG, likely attributed to the temperature gradient and the turbulent effects from an abrupt change in velocity due to the porosity difference. Similarly, turbulent effects may be the cause of the spike in U_{rms} around the boundary between TBT and SAHX. Acoustic power E_{ac}, impedance Z_{ac}, and phase difference between p and U, ϕ_{pU}, are derived from p and U, thus these variables also match closely between CFD and NM. Mean temperature $\overline{T}$ in RT is lower in CFD than NM. CFD resolves the boundary condition at 298 K, whereas NM does not consider heat transfer outside heat exchangers. Furthermore, CFD results demonstrate the capture of changes within the components, such as the temperature distributions across the heat exchangers, which are assumed as constants by NM. These results demonstrate the capability of CFD to accurately resolve the flow field and highlight its potential to handle more complex cases with higher non-linear behaviours. These verify the user case of CFD in optimising the system at a component level.

Other results produced by both CFD and NM, including frequency f, change in acoustic power across the engine cascade ΔE_{ac}, and thermal power inputs to heat exchangers Q, are tabulated in Tab. 6. The difference in frequency is mainly due to the variation in temperature along RT, which affects the speed of sound by around 5 %. The other results show a greater difference; thus, further investigations into the configurations of heat transfer parameters across solid and fluid domains in porous media are needed.

4. CONCLUSIONS

In this article, we explored the potential and necessity of developing and simulating thermoacoustic systems using CFD. Through an investigation of a sample case involving a thermoacoustic engine, we could determine best practices for meshing the system, identifying porous media equations, and formulating their parameters in constructing a CFD model. In this particular CFD study,

- the optimal cell number is 18×10^4, corresponding to grid lengths of 1.0×10^{-3} m at core components and 1.5×10^{-3} m at RTs, with boundary cells refined to around 1.5×10^{-4} m;
- transient behaviours of the onset process are observed, and the system stabilises at a mean pressure of 3.11×10^6 Pa around $t = 20$ s, with non-sinusoidal oscillations of the cross-sectional averaged variables and non-linear behaviour of variables across the components;
- the axial distributions of CFD results closely match the equivalent NM constructed using the same averaged fluid temperatures, suggesting that the flow field is correctly resolved;
- CFD can capture higher levels of detail than NM in all variables;
- the CFD results demonstrate greater heat inputs, implying the potential for further investigations.

ACKNOWLEDGEMENT

This work was performed using resources provided by the Cambridge Service for Data Driven Discovery (CSD3) operated by the University of Cambridge Research Computing Service (www.csd3.cam.ac.uk), provided by Dell EMC and Intel using Tier-2 funding from the Engineering and Physical Sciences Research Council (capital grant EP/T022159/1), and DiRAC funding from the Science and Technology Facilities Council (www.dirac.ac.uk).

The author acknowledges the insightful discussions on computation and thermoacoustics with Peter Benie, Caleb Li, Jingquan Zheng, Matthew Yoko, Ekrem Ekici, Shiyao Ni, Yutao Zheng, and Dr. Francesca De Domenico.

REFERENCE

[1] Swift GW. Thermoacoustics: A Unifying perspective for some engines and refrigerators: Second edition. Cham: Springer International Publishing; 2017

[2] De Blok K. Novel 4-Stage Traveling Wave Thermoacoustic Power Generator. *ASME 2010 3rd Joint US-European Fluids Engineering Summer Meeting*. FEDSM-ICNMM2010. Montréal, Canada; 2010:FEDSM–ICNMM2010–30527

[3] Brown JS, Domanski PA. Review of alternative cooling technologies. Applied Thermal Engineering. 2014; 64:252–62

[4] Tartibu L. Developing more efficient travelling-wave thermo-acoustic refrigerators: A review. Sustainable Energy Technologies and Assessments. 2019; 31:102–14

[5] Zhao Y, Yang Z, Luo E, Zhou Y. Travelling-wave thermoacoustic high-temperature heat pump for industrial waste heat recovery. Energy. 2014; 77:397–402

[6] Xu J, Zhang L, Hu J, Wu Z, Bi T, Dai W, Luo E. An efficient looped multiple-stage thermoacoustically-driven cryocooler for liquefaction and recondensation of natural gas. Energy. 2016; 101:427–33

[7] Xu J, Yu G, Zhang L, Dai W, Luo E. Theoretical analysis of two coupling modes of a 300-Hz three-stage thermoacoustically driven cryocooler system at liquid nitrogen temperature range. Applied Energy. 2017; 185:2134–41

[8] Chi J, Yang Y, Wu Z, Yang R, Li P, Xu J, Zhang L, Hu J, Luo E. Numerical and experimental investigation on a novel heat-driven thermoacoustic refrigerator for room-temperature cooling. Applied Thermal Engineering. 2023; 218:119330

[9] Xu J, Luo E, Hochgreb S. Study on a heat-driven thermoacoustic refrigerator for low-grade heat recovery. Applied Energy. 2020; 271:115167

[10] Chi J, Xu J, Zhang L, Wu Z, Hu J, Luo E. Study of a gas-liquid-coupled heat-driven room-temperature thermoacoustic refrigerator with different working gases. Energy Conversion and Management. 2021; 246:114657

[11] Yang R, Meir A, Ramon GZ. Theoretical performance characteristics of a travelling-wave phase-change thermoacoustic engine for low-grade heat recovery. Applied Energy. 2020; 261:114377

[12] Yang R, Blanc N, Ramon GZ. Environmentally-sound: An acoustic-driven heat pump based on phase change. Energy Conversion and Management. 2021; 232:113848

[13] Clark JP, Ward WC, Swift GW. Design environment for low-amplitude thermoacoustic energy conversion (DeltaEC). 2007

[14] Lycklama à Nijeholt JA, Tijani MEH, Spoelstra S. Simulation of a traveling-wave thermoacoustic engine using computational fluid dynamics. The Journal of the Acoustical Society of America. 2005; 118:2265–70

[15] Yu GY, Luo EC, Dai W, Hu JY. Study of nonlinear processes of a large experimental thermoacoustic-Stirling heat engine by using computational fluid dynamics. Journal of Applied Physics. 2007; 102:074901

[16] Liu L, Liu Y, Duan F. Effect of the characteristic time on the system performance of a three-stage looped traveling-wave thermoacoustic engine. Energy Conversion and Management. 2020; 224:113367

[17] Sun D, Luo K, Zhang J, Yu YS, Pan H. A novel non-linear one-dimensional unsteady model for thermoacoustic engine and its application on a looped traveling-wave thermoacoustic engine. Applied Acoustics. 2021; 181:108136

[18] Baker TJ. Fluent User's Guide. 2019

[19] Abrahamson J. Fluent Theory Guide. 2019

[20] Swift GW, Ward WC. Simple harmonic analysis of regenerators. Journal of Thermophysics and Heat Transfer. 1996; 10:652–62

[21] Shah RK, London AL. Laminar flow forced convection in ducts: a source book for compact heat exchanger analytical data. Advances in heat transfer : Supplement 1. New York: Academic Press; 1978

[22] Rott N. Damped and thermally driven acoustic oscillations in wide and narrow tubes. Zeitschrift für angewandte Mathematik und Physik ZAMP. 1969; 20:230–43

[23] Cho TY, Xu J, Luo E, Hochgreb S. A thermoacoustic refrigerator with a compact thermal buffer tube. *Energy Proceedings*. ICAE2022. Vol. 29. Closing Carbon Cycles – A Transformation Process Involving Technology, Economy, and Society: Part IV. Bochum, Germany; 2022